

WISEA J083011.95+283716.0: A Missing Link Planetary-Mass Object

DANIELLA C. BARDALEZ GAGLIUFFI,¹ JACQUELINE K. FAHERTY,¹ ADAM C. SCHNEIDER,² AARON MEISNER,³
DAN CASELDEN,⁴ GUILLAUME COLIN,⁵ SAM GOODMAN,⁵ J. DAVY KIRKPATRICK,⁶ MARC J. KUCHNER,⁷ JONATHAN GAGNÉ,⁸
SARAH E. LOGSDON,³ ADAM J. BURGASSER,⁹ KATELYN ALLERS,¹⁰ JOHN DEBES,¹¹ JOHN WISNIEWSKI,¹²
AUSTIN ROTHERMICH,¹³ NIKOLAJ S. ANDERSEN,¹⁴ MELINA THÉVENOT,⁵ AND JIM WALLA⁵
BACKYARD WORLDS: PLANET 9 COLLABORATION

¹American Museum of Natural History, 200 Central Park West, New York, NY 10024, USA

²School of Earth and Space Exploration, Arizona State University, 781 Terrace Mall, Tempe, AZ 85287, USA

³NSF's National Optical-Infrared Astronomy Research Laboratory, 950 N Cherry Ave, Tucson, AZ 85719, USA

⁴Gigamon Applied Threat Research, 619 Western Avenue, Suite 200, Seattle, WA 98104, USA

⁵Backyard Worlds: Planet 9

⁶IPAC, Mail Code 100-22, Caltech, 1200 E. California Blvd., Pasadena, CA 91125, USA

⁷NASA Goddard Space Flight Center, Exoplanets and Stellar Astrophysics Laboratory, Code 667, Greenbelt, MD 20771, USA

⁸Institut de Recherche sur les Exoplanètes, Université de Montréal, Pavillon Roger-Gaudry, PO Box 6128 Centre-Ville STN, Montreal QC H3C 3J7, Canada

⁹Center for Astrophysics and Space Sciences, University of California, San Diego, 9500 Gilman Drive, Mail Code 0424, La Jolla, CA 92093, USA

¹⁰Physics and Astronomy Department, Bucknell University, 701 Moore Ave, Lewisburg, PA 17837, USA

¹¹Space Telescope Science Institute, Baltimore, MD 21218, USA

¹²Homer L. Dodge Department of Physics and Astronomy, University of Oklahoma, 440 West Brooks Street, Norman, OK 73019, USA

¹³Physics Department, University Of Central Florida, 4000 Central Florida Boulevard, Building 12, 310, Orlando, FL 32816, USA

¹⁴Kolding Hospital, Department of Cardiology, Sygehus Lillebalt 24, 6000 Kolding, Denmark

(Received; Revised; Accepted April 29, 2020)

Submitted to ApJ

ABSTRACT

We present the discovery of WISEA J083011.95+283716.0, the first Y dwarf candidate identified through the Backyard Worlds: Planet 9 citizen science project. We identified this object as a red, fast-moving source with a faint *W2* detection in multi-epoch *AllWISE* and *unWISE* images. We have characterized this object with *Spitzer* and *Hubble Space Telescope* follow-up imaging. With mid-infrared detections in *Spitzer*'s *ch1* and *ch2* bands and flux upper limits in *HST F105W* and *F125W* filters, we find that this object is both very faint and has extremely red colors ($ch1 - ch2 = 3.25 \pm 0.23$ mag, $F125W - ch2 \geq 9.36$ mag), consistent with a $T_{eff} \sim 300$ K source, as estimated from the known Y dwarf population. A preliminary parallax provides a distance of $11.1_{-1.5}^{+2.0}$ pc, leading to a slightly warmer temperature of ~ 350 K. The extreme faintness and red *HST* and *Spitzer* colors of this object suggest it may be a link between the broader Y dwarf population and the coldest known brown dwarf WISE J0855–0714, and highlight our limited knowledge of the true spread of Y dwarf colors. We also present four additional Backyard Worlds: Planet 9 late-T brown dwarf discoveries within 30 pc.

Keywords: (stars:) brown dwarfs, Y brown dwarfs, Hubble photometry, Space telescopes, Near infrared astronomical observations

1. INTRODUCTION

With temperatures below ~ 500 K, Y dwarfs are the coldest products of star formation (Cushing et al. 2011), and are well within the temperature and mass

range of old giant planets. Detecting Y dwarfs was a key goal of the *Wide Field Infrared Survey Explorer* (*WISE*; Wright et al. 2010), with a mid-infrared filter designed specifically to cover the flux peak of these objects ($\lambda_{W2} = 4.6 \mu\text{m}$). Several discoveries from this mission have reshaped the landscape of the solar neighborhood: WISE J085510.83–071442.5 (hereafter: WISE J0855–0714), the fourth closest system to the Sun ($2.31 \pm 0.08 \text{ pc}$; Luhman & Esplin 2014) and the coldest known brown dwarf to date at $\sim 250 \text{ K}$ (Luhman 2014); WISE J104915.57?531906.1, the closest brown dwarf binary to the Sun, also at 2 pc ($2.02 \pm 0.019 \text{ pc}$; Boffin et al. 2014); and WISE J072003.20–084651.2AB, an M9+T5 dwarf spectral binary system at 6 pc , which traversed the Oort cloud about 70,000 years ago at only 0.25 pc (Scholz 2014; Burgasser et al. 2015; Mamajek et al. 2015), and whose T dwarf component is more massive than predicted from evolutionary models (Dupuy et al. 2019). More recent discoveries have capitalized on multi-epoch *WISE* photometry to reach fainter objects than previous detection thresholds allowed, like the $\sim 270 - 360 \text{ K}$ Y dwarf CWISEP J193518.59–154620.3 (hereafter: CWISEP J1935–1546; Marocco et al. 2019), and the $\sim 310 - 360 \text{ K}$ CWISEP J144606.62–231717.8 (hereafter: CWISEP J1446–2317) (Marocco et al. 2020; Meisner et al. 2020). Nevertheless, the currently known Y dwarf population remains small, totaling only 28 objects (Cushing et al. 2011; Luhman et al. 2011; Liu et al. 2012; Kirkpatrick et al. 2012; Tinney et al. 2012; Kirkpatrick et al. 2013; Luhman 2014; Pinfield et al. 2014; Tinney et al. 2014; Dupuy et al. 2015; Schneider et al. 2015; Martin et al. 2018; Tinney et al. 2018; Marocco et al. 2019, 2020).

Even with this small sample, Kirkpatrick et al. (2019) placed initial constraints on the field luminosity and mass functions of brown dwarfs at cold temperatures. This study found that a single power law mass function extending down to $5 M_{\text{Jup}}$ provided a good fit to the number density of nearby brown dwarfs. However, sampling is particularly sparse at the lowest temperatures, with WISE J0855–0714 being the only object in the $150 - 300 \text{ K}$ temperature range. A larger volume-limited sample of Y dwarfs is needed to improve the statistical measurement of the luminosity function at these temperatures, in order to constrain the low-mass limit of star formation (Burgasser 2004). Similarly, a statistical sample of Y dwarfs is needed to characterize the composition, structure, and dynamics of low temperature atmospheres (e.g. Skemer et al. 2016; Faherty et al. 2014), and possibly identify spectroscopic markers

of different formation pathways between brown dwarfs and giant planets (e.g. Morley et al. 2019).

Y dwarfs have complex atmospheres that resemble those of giant planets, with deep absorption features from CH_4 , H_2O , and possibly NH_3 (Burrows et al. 2003; Burgasser et al. 2012), and ice water clouds (Morley et al. 2014b). Since they are not outshined by a host star, these objects generally are ideal proxies to conduct exoplanet atmospheric characterization studies. However, due to their intrinsic faintness, objects with spectral types later than Y1 either do not have spectroscopic measurements or poor signal-to-noise data that prevent the clear identification of molecular absorption lines and bands. For example, phosphine, salt, and sulfide clouds, similar to those found in the atmospheres of Jupiter (Visscher et al. 2006), were predicted to affect the mid-infrared spectra of Y dwarfs (Morley et al. 2012). However, phosphine was not identified in the M-band spectrum of the 250 K WISE J0855–0714 (Morley et al. 2018; Skemer et al. 2016), and neither were salt nor sulfide clouds, even though their presence is favored by atmospheric retrieval models (Zalesky et al. 2019). Y dwarfs are prime targets for medium resolution spectroscopy with the *James Webb Space Telescope* (*JWST*) to solidly determine their atmospheric composition.

Despite the growth in the known population of cold brown dwarfs, there remain two brightness and temperature gaps between the majority of the known Y dwarfs, WISE J0855–0714, and gas giants like Jupiter ($\sim 125 \text{ K}$; Hanel et al. 1981). To look for the faintest objects missed in previous searches, the Backyard Worlds: Planet 9 citizen science project (BYW:P9) is harnessing the power of visual inspection of multi-epoch and multi-wavelength imaging. The goal of this project is to identify the faintest, coldest, and fastest-moving sources in the Solar neighborhood through time-resolved WISE coadded animations (unWISE; Meisner et al. 2017a,b, 2018a). BYW:P9 was launched in February 2017 (Kuchner et al. 2017) as part of the Zooniverse ecosystem. Since then, over 150,000 users around the world have participated in the visual identification and classification of new brown dwarf candidates through the Backyard Worlds interface¹. Prior discoveries include the lowest binding energy ultracool binary in the field (Faherty et al. 2019), a white dwarf with infrared excess (Debes et al. 2019), and two T-type subdwarfs (Schneider et al., submitted).

In this paper, we present the discovery and space-based follow-up observations of 5 new low-temperature

¹ www.BackyardWorlds.org

brown dwarfs identified by Backyard Worlds: Planet 9 citizen scientists, including one Y dwarf. Section 2 describes the five targets of our sample. Section 3 describes the observations with the *Hubble* and *Spitzer* space telescopes and our photometric measurements. Section 4 shows our parallax calculation and estimated quantities based on our infrared color analysis. Section 5 discusses the implications of our discoveries for our understanding of the T/Y transition, the census of the Solar neighborhood, and brown dwarf formation at the lowest masses.

2. TARGET SAMPLE

The *WISE* observing strategy consists of scanning the entire sky every six months, with over 12 exposures per visit. Co-adding exposures from the full cryogenic *WISE* (Wright et al. 2010), NEOWISE (Mainzer et al. 2011), and NEOWISE Reactivation missions (NEOWISER; Mainzer et al. 2014), led to the generation of full-depth, “unWISE” images in *W1* and *W2* filters (Meisner et al. 2017b, 2018a). These images reach ~ 1.3 mag fainter than single exposures, and are used for the identification of faint, fast-moving sources through BYW:P9.

Our sample contains five sources identified by citizen scientists from the BYW:P9 collaboration due to their red color in $W1 - W2$ and fast proper motion in the 5.5-year baseline of unWISE images (Meisner et al. 2018a,b). None of these objects are detected in the near-infrared Two Micron All Sky Survey (2MASS; Skrutskie et al. 2006), the UKIRT Hemisphere Survey (UHS; Dye et al. 2018), or the VISTA Hemisphere Survey (VHS; McMahon et al. 2013). In the mid-infrared, our five sources have only flux upper limit AllWISE photometry in *W1* and detections with large uncertainties in *W2*, leading to uncertain $W1 - W2$ colors that nevertheless indicate extremely faint and red objects.

The precision and accuracy of the photometry and proper motions of these objects are significantly improved in the CatWISE Preliminary catalog (Eisenhardt et al. 2019) relative to AllWISE. CatWISE is a new catalog resulting from running the AllWISE software on unWISE images using NEOWISE epochs, yielding 10X better per-coordinate proper motion uncertainty at $W1 \sim 15$ mag, and is 3 magnitudes more sensitive than AllWISE at 100 mas/yr . Since AllWISE proper motions are generally unreliable at $W2 \geq 13.5$ mag (Kirkpatrick et al. 2016), and have been superseded by CatWISE, we present only CatWISE photometry and proper motions in Table 1 and use these measurements in the analysis that follows.

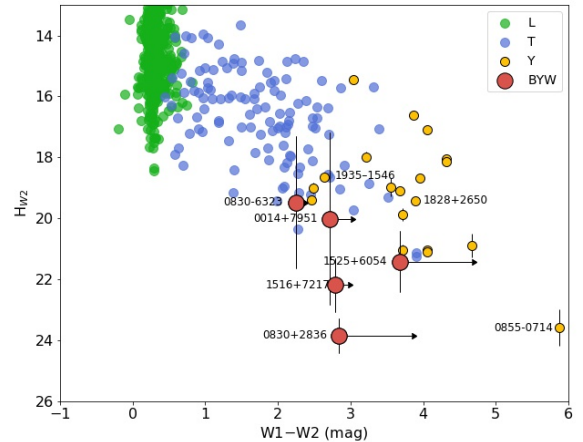


Figure 1. Reduced proper motion diagram in *W2* band from AllWISE. All five objects in our sample are flux upper limits in *W1* from AllWISE. Background M, L, and T dwarfs come from Faherty et al. (2009, 2012). Y dwarfs are compiled from Kirkpatrick et al. (2019).

Using multi-epoch unWISE data (Meisner et al. 2018a), we measured proper motions for each source and placed them in a reduced proper motion diagram, traditionally used to distinguish faint main sequence stars from subdwarfs and cool, white dwarfs if parallaxes are absent, acting as a proxy for absolute magnitude (Luyten 1922). For our BYW:P9 *HST* follow-up, we prioritized five sources that overlap with the known Y dwarf population (see Figure 1). These sources were also observed as part of our *Spitzer* follow-up program. In the next sections, we characterize these sources with both sets of photometry.

3. OBSERVATIONS

3.1. WFC3/HST Photometry

Our targets were observed between UT 11 August 2018 and UT 16 February 2019 in 5 *HST* orbits under GO program 15468 (PI: Faherty). All five targets were observed with both F105W ($\lambda_c = 1055.2$ nm) and F125W ($\lambda_c = 1248.6$ nm) filters on the Wide Field Camera 3 (WFC3; MacKenty et al. 2008), which roughly coincide with the *Y* and *J* near-infrared bands. All of the observations were done in MULTIACUUM mode with 4 dither positions per source per filter in a $123'' \times 135''$ field of view. Total exposure times are listed in Table 2. Scheduled observations of WISEA J1516+7217 on UT 2018 November 5 were taken on gyros only, after failing to acquire a guide star, but these were rescheduled and successfully acquired on UT 2019 February 16. The individual exposures per filter were combined, cleaned

Table 1. CatWISE photometry and proper motions.

| Source | CatWISE Designation | W1 (mag) | W2 (mag) | W1 – W2 (mag) | μ_α (mas/yr) | μ_δ (mas/yr) | μ_{total} (mas/yr) |
|----------------------------|----------------------------|------------|--------------|---------------|-----------------------|-----------------------|------------------------|
| WISEA J001449.96+795116.1 | CWISEP J001450.72+795116.0 | 18.72±0.28 | 16.00±0.06 | 2.72±0.28 | 531.2±89.2 | -20.7±77.8 | 531.6±89.2 |
| WISEA J083011.95+283716.0* | CWISEP J083011.94+283716.2 | ≥18.0 | 16.639±0.188 | ≥1.33 | -730.40±290.7 | -1161.20±367.0 | 1371.43±468.18 |
| | CWISEP J083011.94+283706.1 | ≥18.9 | 16.052±0.092 | ≥2.9 | 54.3±153.5 | -314.3±154.1 | 319.0±154.1 |
| WISEA J083019.97–632305.4 | CWISEP J083019.95-632304.2 | 18.12±0.10 | 15.87±0.04 | 2.25±0.10 | -81.7±65.4 | 375.0±64.7 | 383.8±64.7 |
| WISEA J151620.39+721745.4 | CWISEP J151620.00+721747.9 | 18.91±0.17 | 16.13±0.05 | 2.79±0.18 | -562.2±89.9 | 560.8±78.9 | 794.1±84.5 |
| WISEA J152529.09+605356.5 | CWISEP J152528.90+605359.0 | ≥19.7 | 15.99±0.05 | ≥3.7 | -394.2±85.1 | 763.7±85.6 | 859.4±85.5 |

* Two CatWISE entries are found when searching for the AllWISE source WISEA J083011.95+283716.0. This object has such a high proper motion that the CatWISE pipeline confused it as two sources. The photometry and proper motion reported in CatWISE for this object are unreliable. Our *Spitzer* photometry (Table 3) and astrometry (Table 4) supersede the values reported in this Table for this object.

NOTE—Object names are from AllWISE, magnitudes and proper motions are updated from CatWISE. For CatWISE, we report photometry from the `w1mpro.pm` and `w2mpro.pm` keywords and their associated uncertainties.

of cosmic rays, and registered to the World Coordinate System (WCS) with the `tweakreg` and `astrodrizzle` routines available in the AstroDrizzle software (Gonzaga et al. 2012).

Photometry was calculated on the drizzled images using a custom function² built with routines from the `photutils` Python package. Centroids were determined using the `DA0StarFinder` Python routine based on the DAOFIND algorithm (Stetson 1987). This algorithm uses a 2D Gaussian kernel to search for local maxima with a peak amplitude greater than a given threshold. We chose a full-width half maximum of 3 pixels and a threshold of 5 times the median absolute deviation in a 50-by-50 pixel cut-out of the science images centered on the targets. This method yielded more accurate results than other 1-D and 2-D Gaussian fitting techniques (e.g., `photutils.centroids`).

WFC3 pixels become correlated after the drizzling process, so rather than calculating the background flux with an annulus around the target, we followed the prescription of Schneider et al. (2015). The contribution of the sky background was estimated by randomly placing 10,000 apertures on the image, and calculating aperture photometry on them. The radius for these apertures was 0''.4 in flux units of e^-/s , thus matching the one used for aperture photometry on the sources, as defined in the *WFC3* Data Handbook (Gennaro, M. et al. 2018). The array of background count values was sigma-clipped to 3σ to avoid contribution from apertures containing stars or anomalous negative-count pixels. The median and standard deviation of the background are used as the value and uncertainty in the sky contribution.

Aperture photometry on the stellar sources was calculated using the same radius of 0''.4. The final source

flux was obtained by subtracting the background flux from the aperture flux, since both aperture areas were the same. Magnitudes in the Vega system were directly calculated from the fluxes using zero points of 25.4523 mag and 25.1439 mag for the F105W and F125W filters, respectively, as defined by the *HST*/WFC3 data handbook (Gennaro, M. et al. 2018). Uncertainties on the stellar flux were estimated following the DAOPHOT photometry error method (Stetson 1987) and includes Poisson error contributions from stellar and background counts and read error from the detector:

$$\sigma_{tot} = \frac{\sqrt{\frac{F\Delta t_{exp}}{geff} + A(\sigma_{bkg}\Delta t_{exp})^2 + A^2\frac{(\sigma_{bkg}\Delta t_{exp})}{N_{sky}}}}{\Delta t_{exp}} \quad (1)$$

where F is the raw aperture flux (including both stellar and background contributions), Δt_{exp} is the exposure time, $geff$ is the effective gain, A is the aperture area, σ_{bkg} is the standard deviation of the background in e^-/s , and N_{sky} is the number of sky pixels used to estimate the background. Since the WFC3 images come in units of e^-/s , the effective gain can be estimated as the total exposure time³, as extracted from the FITS headers. For a total uncertainty per pixel per second, this equation can be reduced to:

$$\sigma_{tot} = \sqrt{\frac{F}{\Delta t_{exp}} + 2\sigma_{bkg}^2} \quad (2)$$

For the case of WISEA J0830+2837, which is undetected in both *HST* filters, we estimate a 3σ upper limit on flux from the standard deviation of the flux from the 10,000 background apertures.

² Found at <https://github.com/daniellabardalezgagliuffi/HSTphotometry>

³ See https://photutils.readthedocs.io/en/stable/api/photutils.utils.calc_total_error.html for more details.

Table 2. Summary of *HST* and *Spitzer* observations.

| Source | R.A. | Dec. | Obs. Date | Total Exp. Time (s) | Filter |
|------------------|-------------|--------------|-------------|---------------------|--------|
| <i>HST</i> | | | | | |
| WISEA J0014+7951 | 00 15 01.32 | +79 51 08.08 | 2018 Aug 11 | 1412 | F105W |
| | | | | 1412 | F125W |
| WISEA J0830+2837 | 08 30 11.89 | +28 36 58.23 | 2018 Sep 29 | 1212 | F105W |
| | | | | 1312 | F125W |
| WISEA J0830-6323 | 08 30 19.95 | -63 22 59.97 | 2018 Aug 29 | 1312 | F105W |
| | | | | 1412 | F125W |
| WISEA J1516+7217 | 15 16 19.43 | +72 17 53.81 | 2019 Feb 16 | 1412 | F105W |
| | | | | 1412 | F125W |
| WISEA J1525+6053 | 15 25 28.65 | +60 54 03.32 | 2018 Nov 5 | 1312 | F105W |
| | | | | 1412 | F125W |
| <i>Spitzer</i> | | | | | |
| WISEA J0014+7951 | 00 14 49.96 | +79 51 16.2 | 2018 Dec 16 | 378 | ch1 |
| | | | | 378 | ch2 |
| WISEA J0830+2837 | 08 30 11.96 | +28 37 16.0 | 2019 Feb 21 | 378 | ch1 |
| | | | | 378 | ch2 |
| WISEA J0830-6323 | 08 30 19.98 | -63 23 05.5 | 2018 Aug 14 | 378 | ch1 |
| | | | | 378 | ch2 |
| WISEA J1516+7217 | 15 16 20.40 | +72 17 45.5 | 2019 Feb 11 | 378 | ch1 |
| | | | | 378 | ch2 |
| WISEA J1525+6053 | 15 25 29.10 | +60 53 56.6 | 2018 Oct 21 | 378 | ch1 |
| | | | | 378 | ch2 |

The *HST* images of WISEA J0014+7951 reveal a nearby fainter source $1''2$ away at a position angle of 231.52° East of North. We measured $F105W$ and $F125W$ magnitudes of 24.07 ± 0.265 mag and 23.59 ± 0.271 mag, respectively, leading to an *HST* color of 0.48 ± 0.38 mag. This source is ~ 3 mag fainter than our WISEA J0014+7951 target in both bands ($F105W = 20.924 \pm 0.015$ mag, $F125W = 19.993 \pm 0.008$ mag), and its *HST* color is roughly half a magnitude bluer than the *HST* color of WISEA J0014+7951 ($F105W - F125W = 0.931 \pm 0.017$ mag, see Table 3). We hypothesize, that if this object were a true companion to the T8 WISEA J0014+7951, by definition it would be cooler, later-type, and hence redder (c.f. Schneider et al. 2015, 2016; Kirkpatrick et al. 2019). However, given the bluer *HST* color, it is unlikely that these two objects are associated. Unfortunately, these two sources are blended in our *Spitzer* images, so we are unable to measure a second color to better characterize this object.

3.2. *Spitzer* photometry

In addition to the *HST* photometry, we also obtained *Spitzer* photometry for these five targets, as part of program ID 14076 (PI: Faherty). The observations followed a 16-point spiral dither pattern with 30 s exposures per

frame. Data were acquired with both *ch1* and *ch2* filters. Readout was done in full array mode.

Aperture photometry was measured using the *Spitzer* MOsaicker and Point Source EXtractor with point-source extraction package (MOPEX/APEX; Makovoz & Marleau 2005), and can be found in Table 2. Specifically, we used the corrected basic calibrated data (CBCD) frames to build custom mosaics from which the fluxes were measured using a 4-pixel aperture. These raw fluxes were converted to magnitudes by applying an aperture correction and comparing to the published *ch1* and *ch2* flux zero points, as described in section 5.1 of Kirkpatrick et al. (2019).

4. ANALYSIS

4.1. Preliminary parallax of WISEA J0830+2837

Spitzer ch2 imaging of WISEA J0830+2837 was obtained in 2019 Feb via program 14076 (PI: Faherty) and in 2019 Jul-Aug via program 14224 (PI: Kirkpatrick). Astrometry was measured from the *Spitzer* images using the methodology described in section 5.2 of Kirkpatrick et al. (2019) with a couple of exceptions. First, we used re-registration stars sampling down to smaller S/N values (S/N=30) in order to have a larger selection of objects per frame that match *Gaia* DR2 sources with full astrometric solutions. Second, we used the

Table 3. *HST* and *Spitzer* photometry.

| Parameter | WISEA J0014+7951 | WISEA J0830+2837 | WISEA J0830-6323 | WISEA J1516+7217 | WISEA J1525+6053 |
|--------------------------------------------------|------------------|------------------|------------------|------------------|------------------|
| <i>HST</i> Ap. <i>F105W</i> (mag) | 20.924±0.015 | ≥25.4 | 20.225±0.010 | 21.470±0.013 | 21.173±0.013 |
| <i>HST</i> Ap. <i>F125W</i> (mag) | 19.993±0.008 | ≥25.2 | 19.297±0.004 | 20.557±0.007 | 20.233±0.006 |
| <i>HST</i> Ap. <i>F105W</i> - <i>F125W</i> (mag) | 0.931±0.017 | — | 0.928±0.011 | 0.913±0.015 | 0.940±0.014 |
| <i>Spitzer</i> PRF <i>ch1</i> (mag) | 17.727±0.068 | 19.089±0.232 | 17.514±0.058 | 18.121±0.096 | 18.000±0.084 |
| <i>Spitzer</i> PRF <i>ch2</i> (mag) | 15.880±0.021 | 15.837±0.021 | 15.682±0.019 | 15.946±0.021 | 15.874±0.021 |
| <i>Spitzer</i> PRF <i>ch1</i> - <i>ch2</i> (mag) | 1.847±0.071 | 3.252±0.233 | 1.832±0.061 | 2.175±0.098 | 2.126±0.087 |
| <i>Spitzer</i> Ap. <i>ch1</i> (mag) | 17.777±0.050 | 19.110±0.166 | 17.479±0.040 | 18.220±0.072 | 18.048±0.063 |
| <i>Spitzer</i> Ap. <i>ch2</i> (mag) | 15.845±0.017 | 15.854±0.018 | 15.669±0.017 | 15.947±0.018 | 15.893±0.018 |
| <i>Spitzer</i> Ap. <i>ch1</i> - <i>ch2</i> (mag) | 1.932±0.053 | 3.256±0.167 | 1.810±0.043 | 2.273±0.074 | 2.155±0.655 |
| Discoverer* | 1, 2, 3, 4, 5, 7 | 1, 2 | 2, 5 | 2 | 2, 6 |

* (1) Dan Caselden; (2) Guillaume Colin; (3) Sam Goodman; (4) Austin Rothermich; (5) Nikolaj Stevnbak; (6) Melina Thevenot; (7) Jim Walla.

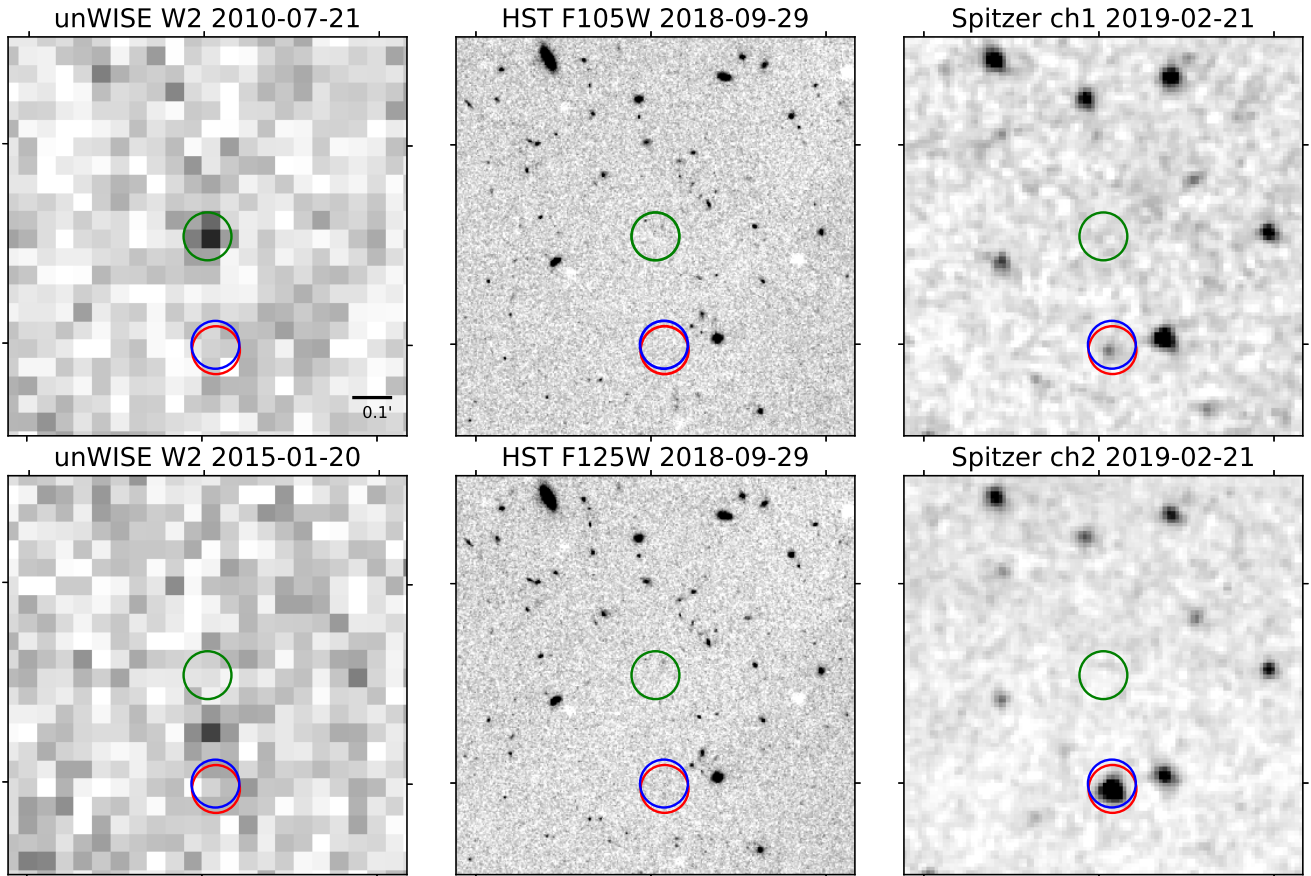


Figure 2. Finder charts for WISEA J0830+2837 of 1 arcminute per side. All frames are centered on the source at the first unWISE epoch (top left) and aligned North up, East to the left. unWISE positions are shown in green, *HST* positions in blue, and *Spitzer* positions in red. Significant proper motion can be seen between the two epochs of unWISE images. For *HST* images, we estimated the location of the source based on the *Spitzer* location and proper motion. The source is significantly brighter in *Spitzer* ch2 compared to ch1, and not detected in the NIR *HST* filters, signaling an extremely cold object.

Table 4. Preliminary *WISE* and *Spitzer* Parallax and Motion Fit for WISE 0830+2837

| Parameter | Value |
|-------------------------------|--------------------|
| RA at t_0 | 127.549578(114.9) |
| Dec at t_0 | 28.617508(74.3) |
| t_0 (MJD) | 57762.10 |
| π_{abs} (mas) | 90.6 \pm 13.7 |
| μ_{RA} (mas yr $^{-1}$) | -233.3 \pm 48.6 |
| μ_{Dec} (mas yr $^{-1}$) | -2040.8 \pm 29.9 |
| χ^2 | 20.370 |
| Dof | 29 |
| Red. χ^2 | 0.702 |

full astrometric solutions of these re-registration stars to place each frame on an absolute astrometric grid – that is, we move each *Gaia* source to its expected position at that epoch and re-register the frame to that epoch-specific reference. This enables us to measure an absolute parallax, obviating the need to apply an ad hoc relative-to-absolute adjustment later.

After the original photometric follow-up in program 14076, we had only one additional visibility window available to us in program 14224 with which to measure astrometry for this object, because the *Spitzer* mission ceased operations on 30 Jan 2020. The data from programs 14076 and 14224 sample opposite sides of the parallactic ellipse, since they are separated by ~ 6 months, but at least one other epoch of data is needed to disentangle proper motion from parallax. We therefore used source detections from the unWISE epochal coadds (Lang 2014) in a region around WISE 0830+2837, re-registered their positions to the *Gaia* DR2 reference frame, and used the resulting re-registered unWISE astrometry to provide eleven additional epochs spanning Apr 2010 to Oct 2018. (See Meisner et al. 2020 for more details on the process.) These unWISE data were then associated with the appropriate XYZ position of the Earth at the mean time of each of the eleven unWISE epochs in the ICRS reference frame. A combined proper motion + parallax solution was fit using the methodology outlined in Section 5.2.3 of Kirkpatrick et al. (2019).

Our resulting solution is given in Table 4 and illustrated in Figure 3. The parallactic solution should be considered preliminary and somewhat fragile because there is a single high-quality data point anchoring one side of the parallactic ellipse. This is further demonstrated by the large parallactic error of $\sim 15\%$.

We find that the parallax is 90.6 ± 13.7 mas, implying a distance of $11.1_{-1.5}^{+2.0}$ pc. This parallax indicates an absolute magnitude in *ch2* of 15.61 ± 0.05 mag, which leads to a temperature range of 281 – 427 K following the Kirkpatrick et al. (2019) empirical relations.

4.2. Near and Mid-Infrared Colors and Estimated Quantities

Equipped with *HST* and *Spitzer* photometry, we can characterize these objects in the context of other T and Y dwarfs. We have gathered colors from 14 late-T and Y dwarfs with *HST* and *Spitzer* photometry in the literature (Schneider et al. 2015, 2016) and used these as a comparison sample. Figure 4 shows our five targets in *ch1* – *ch2* vs *F125W* – *ch2* color-color space. Based on the colors of the comparison sample, it appears that all the objects in our sample, except for WISEA J0830+2837, are late-T dwarfs. WISEA J0830+2837 appears to be an early-Y dwarf (Table 3, and Figure 5).

Following the Kirkpatrick et al. (2019) relations for absolute magnitude in *ch2*, we estimate distances of 23 – 28 pc for our T dwarf candidates, and $8.7_{-1.9}^{+2.3}$ pc for WISEA J0830+2837, with Monte Carlo uncertainties at the 16th and 84th percentiles. This photometric distance is consistent with the parallax measurement within uncertainties. However, it is worth noting that the empirical relations rely on one data point beyond *ch1* – *ch2* ~ 3.5 mag or $M_{ch2} \sim 16$ mag, corresponding to WISE J0855–0714, hence making any color-based estimation extremely tentative.

From every standpoint, WISEA J0830+2837 is an outlier in our sample. This object is undetected in both *HST* *F105W* and *F125W* filters, thus we only have flux upper limits. In *Spitzer* colors however, this source is detected with moderately large error bars. It is the faintest object in *ch1* in our sample, and the second brightest in *ch2*. The *Spitzer* *ch1* – *ch2* colors for our five targets are in the 1.8 – 2.1 mag range with the exception of WISEA J0830+2837, which has the reddest *ch1* – *ch2* color of the sample (*ch1* – *ch2* = 3.25 ± 0.23 mag). Its color is comparable to CWISEP J1935–1546 (*ch1* – *ch2* = 2.984 ± 0.034 mag, Meisner et al. 2020), and within 1σ of the *Spitzer* color of WISE J0855–0714 (Δ *ch1* – *ch2* = 0.3 ± 0.2 mag). Additionally, from the *Spitzer* colors of WISEA J0830+2837, we can estimate an effective temperature of ~ 300 K for this object (Kirkpatrick et al. 2019), also analogous to CWISEP J1935–1546 with a temperature (270 – 360 K). These two objects appear to be “missing links” filling the gap between most known Y dwarfs and WISE J0855–0714.

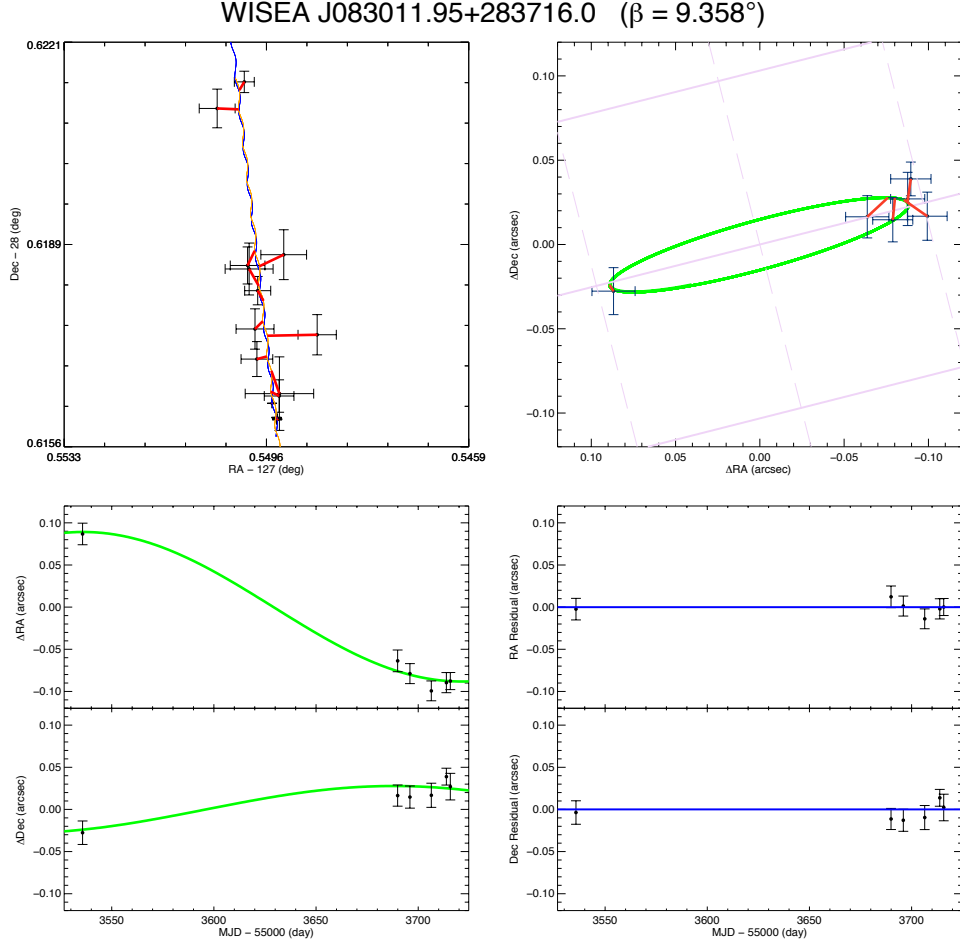


Figure 3. Our fit to the astrometry of WISEA 0830+2837. The full solution and full data sets are shown in the upper left panel, where the unWISE data points are the black points with large error bars and the *Spitzer* data points are the black points with the much smaller error bars. The blue curve is the expected astrometric path of the object as seen from *Spitzer*, and the orange curve is the path as seen from the Earth. Each of the observed data points is connected by a red line back to the spot on the curve that has the same time stamp. The other panels – the parallax-only solution (green curve, upper right), residuals around the parallax solution (lower left), and residuals around the full solution (lower right) – show only the *Spitzer* data points, for clarity.

Based on parallax and proper motion of WISEA J0830+2837 fore, WISEA J0830+2837 is likely a planetary-mass object. with *Spitzer*, we can estimate a tangential velocity of $V_{tan} = 107.9 \pm 16.67$ km/s, which is significantly higher than the median V_{tan} and velocity dispersion (σ_{tan}) for the nearby T dwarf population (31 km/s and 20 km/s, respectively; Faherty et al. 2012). The V_{tan} of this object is also higher than that of comparable objects, such as the Y dwarf WISE J163940.83?684738.6 (Tinney et al. 2012), with a $V_{tan} = 73 \pm 8$ km/s. The high V_{tan} of WISEA J0830+2837 suggests a kinematically old age. Assuming an age between 1-10 Gyr for this object, we estimate a mass of 4-13 M_{Jup} using the Baraffe et al. (2015) evolutionary models. There-

object.

5. DISCUSSION

5.1. The low mass end of the substellar IMF

As shown in Figure 6, WISEA J0830+2837 is one of the faintest and reddest objects in the Y dwarf population. Similar in brightness and *Spitzer* color are CWISEP J1935–1546 (Marocco et al. 2019) and CWISEP J1446–2317 (Marocco et al. 2020; Meisner et al. 2020). These three objects constitute a small sample bridging the known Y dwarf population to WISE J0855–0714 (Luhman 2014). Constraining the initial mass function (IMF) observationally is crucial

Table 5. Estimated physical properties of our sample based on *Spitzer* colors and parallax measurement for WISEA J0830+2837.

| Source | Photometric Type | T_{eff} (K) | Distance (pc) |
|------------------|------------------|----------------------|----------------------|
| WISEA J0014+7951 | T8 | 659 ± 85 | 28 ± 4 |
| WISEA J0830+2837 | $\geq Y1$ | 303 ± 87 | 9 ± 2 |
| | $\geq Y1^*$ | $354 \pm 73^*$ | $11.1^{+2.0}_{-1.5}$ |
| WISEA J0830-6323 | T8 | 664 ± 84 | 26 ± 4 |
| WISEA J1516+7217 | T9 | 548 ± 87 | 24 ± 4 |
| WISEA J1525+6053 | T9 | 563 ± 86 | 24 ± 4 |

* Calculated distance, and estimated photometric type and effective temperature from *Spitzer* parallax measurement.

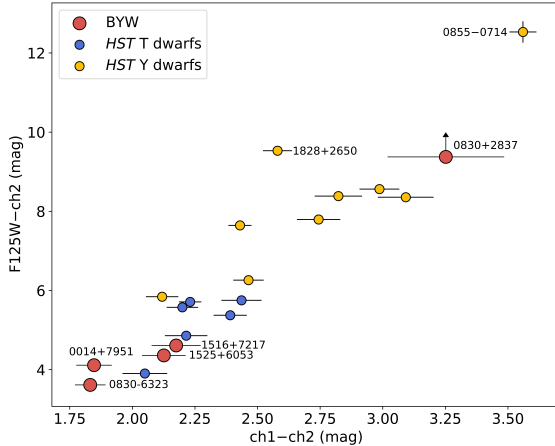


Figure 4. Color-color diagram of *Spitzer* $ch1-ch2$ color against $F125W-ch2$. Our Backyard Worlds sample is colored in red. *HST* and *Spitzer* photometry for T and Y dwarfs from Schneider et al. (2015, 2016) are shown as blue and yellow circles, respectively. The *Spitzer* photometry of WISEA J0830+2837 places it solidly in the Y-dwarf populated region, with extremely red colors bridging the gap between WISE J0855-0714 and the rest of the Y dwarf population.

to understanding the low-mass limit of brown dwarf formation, and Y dwarfs are the lowest-mass piece in the present-day luminosity function that maps onto an IMF. Perhaps the most fundamental open question in brown dwarf science is how these low-mass objects form. Brown dwarfs most likely form in a process similar to an extension of star formation, i.e. from the gravitational collapse of a molecular cloud. However, the mechanisms leading to an initial collapse at lower masses (e.g. turbulent fragmentation; Padoan & Nordlund 2002), to formation in different locations (e.g. disk fragmentation; Stamatellos & Whitworth 2009), to halt

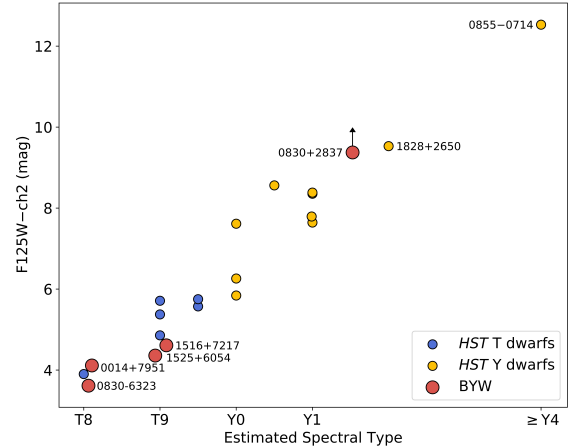


Figure 5. Estimated spectral type vs. *HST* and *Spitzer* color. Our Backyard Worlds/*Spitzer* sample is colored in red. T and Y dwarfs from (Schneider et al. 2016) are shown in blue and yellow, respectively. Error bars for our sample are smaller than the symbol size, on average ~ 0.05 mag.

accretion onto a protostar (e.g. photoevaporation or by ejection of prestellar cores; Whitworth & Zinnecker 2004; Reipurth & Clarke 2001, respectively) have not been fully determined.

The minimum fragmentation mass is determined by the opacity of the gas in a molecular cloud, as high densities cause it to become opaque to its own radiation, and leading to a maximum density at which fragmentation can occur (Low & Lynden-Bell 1976; Rees 1976; Silk 1977a,b). From simple critical Jeans mass arguments (Jeans 1902), Low & Lynden-Bell (1976) derived a minimum fragmentation mass of $7 M_{\text{Jup}}$, not taking into account effects from magnetic fields, rotation, or late accretion. Magneto-hydrodynamical simulations from Bate (2012) which include these effects, as well as turbulence, shock compression, and radiative feedback, find a lower minimum fragmentation mass of $3 M_{\text{Jup}}$ (see also Boyd & Whitworth 2005; Padoan et al. 2005, 2007). Observationally, Kirkpatrick et al. (2019) set an initial constraint on the minimum fragmentation mass of $5 M_{\text{Jup}}$ by fitting a simulated population from evolutionary models to their luminosity functions. However, this result is sensitive to the frequency of coldest Y dwarfs, which only included WISE J0855-0714 at the time of publication. WISEA J0830+2837, CWISEP J1446-2317, and CWISEP J1935-1546 are critical additions to the currently undersampled $T_{\text{eff}} \lesssim 300$ K population, and are essential to confidently constrain the low-mass cutoff of the substellar initial mass function. To see whether the

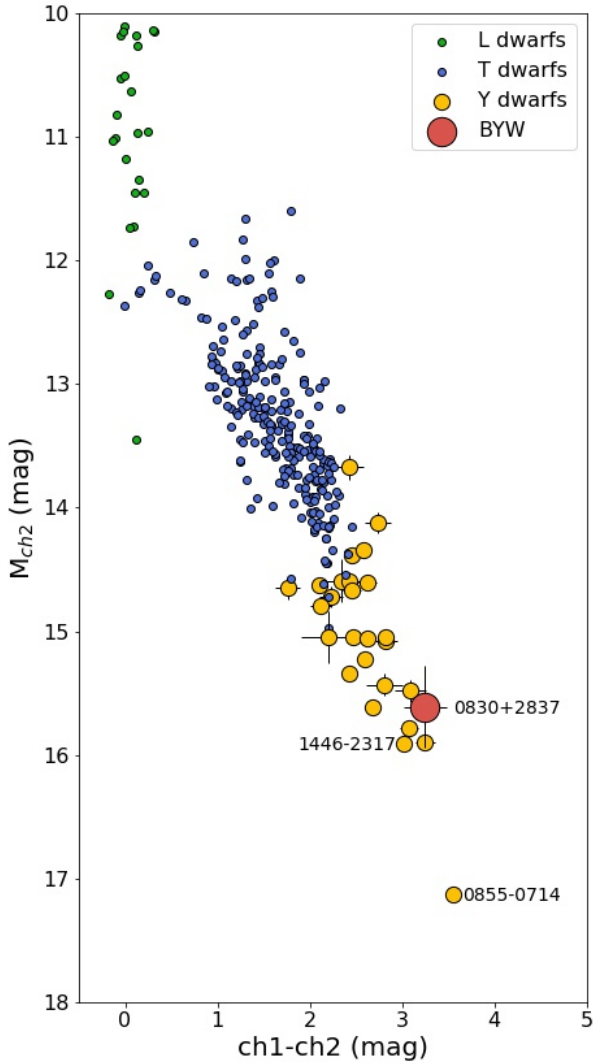


Figure 6. Color-magnitude diagram in *Spitzer* IRAC $ch2$ -band. L dwarf parallaxes and $ch2$ photometry come from the Database of Ultracool Parallaxes Dupuy & Liu (2012); Dupuy & Kraus (2013); Liu et al. (2016); T and Y dwarf parallaxes come from Kirkpatrick et al. (2019). WISEA J0830+2837 joins CWISEP J1935–1546 and CWISEP J1446–2317 on a small, yet growing sample of “missing link” objects bridging the known Y dwarf population to the coldest brown dwarf known, WISE J0855–0714.

theoretically predicted minimum fragmentation masses do indeed describe the observed brown dwarf population, future empirical studies of the initial mass function will need to incorporate the growing sample of “missing link” Y dwarfs. However, such calculations are beyond the scope of this work.

5.2. Characterization of low-temperature atmospheres, from the T/Y dwarf transition to Jupiter

Our sample contains five ultracool dwarfs, one of which connects the population of known Y dwarfs with the coldest brown dwarf ever discovered. The rest of our targets are most likely late-T dwarfs based on the available evidence. WISEA J0830+2837 is the 29th Y dwarf ever discovered, and the first one from the BYW:P9 collaboration. While most Y dwarfs have been spectroscopically confirmed, their intrinsic faintness in NIR leads to poor S/N and an incomplete characterization of their atmospheric composition. The best atmospheric analog for these extremely cold brown dwarfs is Jupiter itself. While T dwarfs have atmospheres rich in methane and water, identified by the deep absorption bands in their near-infrared spectra, Y dwarfs are expected to have water vapor clouds (Morley et al. 2018; Skemer et al. 2016; Faherty et al. 2014). At the T/Y dwarf boundary, Na and K alkalis completely disappear (Zalesky et al. 2019), drastically affecting the $Y - J$ colors at the boundary. At the low temperatures of Y dwarfs, atmospheric models predict the emergence of NH_3 in their NIR spectra (Burrows et al. 2003; Leggett et al. 2007; Lodders & Fegley 2002), and condensation of salt and sulfide clouds (Morley et al. 2012). While tentative ammonia absorption has been observed in the NIR spectrum of an object at the T/Y transition (Burgasser et al. 2012), and NH_3 abundances have been extracted from atmospheric retrievals of Y dwarf NIR spectra as absorption features were attributed to this gas (Zalesky et al. 2019), a conclusive absorption feature matching theoretical predictions is still lacking (e.g., Schneider et al. 2015). Phosphine, which abounds in the Jovian atmosphere at $4.5 - 4.6\mu\text{m}$, was also expected in Y dwarfs. However, mid-infrared spectra of WISE J0855–0714 did not show indications of this molecule (Morley et al. 2018; Skemer et al. 2016). Therefore, we need higher S/N, higher resolution spectra, and/or a broader wavelength coverage, as well as more developed line lists for these molecules, to identify the components of low-temperature atmospheres.

Observationally, the spread in colors currently seen at the T/Y dwarf boundary and throughout the Y dwarf class, could be driven by metallicity, gravity, binarity, cloud coverage, or variability effects. A predicted rever-

sal of NIR color trend from bluer in T-dwarfs to redder in Y-dwarfs (Burrows et al. 2003; Saumon et al. 2012; Morley et al. 2014a) has been confirmed with a spectral energy distribution of WISE J0855–0714 (Luhman & Esplin 2016), and attributed to energy redistribution at longer wavelengths at colder temperatures, and the collapse of the Wien tail (Schneider et al. 2016). Faherty et al. (2014) interpreted their J3-[4.5] color measurement as an indication of water ice and sulfide clouds based on equilibrium chemistry models. On the other hand, Luhman & Esplin (2014) were able to reproduce this color with cloudless, disequilibrium chemistry models, leading to the conclusion that no set of models could simultaneously reproduce the near and mid-infrared photometry (Schneider et al. 2016; Luhman & Esplin 2016). However, Skemer et al. (2016) and Morley et al. (2018) disputed the Luhman & Esplin (2014) result and validated water ice clouds as the interpretation for the absorption features in the 3.4 – 5.2 μm spectra. Finally, photometric variability at a 4% level was detected in WISE J0855–0714 in the mid-infrared (Esplin et al. 2016), suggesting a patchy atmosphere, yet the cloud composition remains unclear.

WISEA J0830+2837, along with CWISEP J1935–1546 and CWISEP 1446–2317, fill an important gap in the Y dwarf sequence to continuously map atmospheric composition across low temperatures down to Jupiter. Atmospheric retrievals on a medium resolution, near-infrared spectrum of this object with NIRSpec aboard the *James Webb Space Telescope* would provide the necessary S/N to identify individual absorption lines and bands to characterize their atmospheres.

6. CONCLUSIONS

We have analyzed *HST* and *Spitzer* photometry of a sample of five ultracool dwarfs identified through the Backyard Worlds: Planet 9 project. We have identified four late-T dwarfs within 30 pc and one of the coldest Y dwarfs ever recorded, WISEA J0830+2837. This source has a solid detection in *ch1* and *ch2* *Spitzer* bands, but it drops out on both *F105W* and *F125W* *HST* bands. These *HST* bands are centered in near-infrared wavelengths, where this cold object no longer emits sufficient flux to be detected, while most of its energy is being emitted in longer, mid-infrared wavelengths to which the *Spitzer* filters are sensitive. WISEA J0830+2837

joins CWISEP J1935–1546 and CWISEP 1446–2317 in a small sample of objects serving as a bridge between WISE J0855–0714 and the known population of Y dwarfs. The Backyard Worlds: Planet 9 citizen science project is proving its efficacy at identifying the coldest brown dwarfs, and will continue to provide exceptional targets for follow-up observations.

We thank our anonymous referee for their helpful and insightful suggestions that have greatly improved the clarity of this paper. The Backyard Worlds: Planet 9 team would like to thank the many Zooniverse volunteers who have participated in this project, from providing feedback during the beta review stage to classifying flipbooks to contributing to the discussions on TALK. We would also like to thank the Zooniverse web development team for their work creating and maintaining the Zooniverse platform and the Project Builder tools. This research was supported by NASA ADAP grant NNH17AE75I. This publication makes use of data products from the Wide-field Infrared Survey Explorer, which is a joint project of the University of California, Los Angeles, and the Jet Propulsion Laboratory/California Institute of Technology, funded by the National Aeronautics and Space Administration. This research has made use of the NASA/IPAC Infrared Science Archive, which is funded by the National Aeronautics and Space Administration and operated by the California Institute of Technology. This research has made use of the VizieR catalogue access tool, CDS, Strasbourg, France (DOI : 10.26093/cds/vizier). The original description of the VizieR service was published in 2000, A&A 143, 23. This research made use of APLpy, an open-source plotting package for Python (Robitaille & Bressert 2012).

Facilities: *HST* (WFC3), *Spitzer* (IRAC), IRSA, AllWISE, CatWISE

Software: APLpy (Robitaille & Bressert 2012), astrodrizzle (Gonzaga et al. 2012), astropy (Astropy Collaboration et al. 2013), MOPEX/APEX (Makovoz & Marleau 2005), Pandas (McKinney 2013), photutils (Bradley et al. 2019), SAOviewerDS9 (Joye & Mandel 2003), WiseView (Caselden et al. 2018).

REFERENCES

- Astropy Collaboration, Robitaille, T. P., Tollerud, E. J., et al. 2013, A&A, 558, A33, A33
- Baraffe, I., Homeier, D., Allard, F., & Chabrier, G. 2015, A&A, 577, A42, A42
- Bate, M. R. 2012, MNRAS, 419, 3115, 3115

- Boffin, H. M. J., Pourbaix, D., Mužić, K., et al. 2014, *A&A*, 561, L4, L4
- Boyd, D. F. A., & Whitworth, A. P. 2005, *A&A*, 430, 1059, 1059
- Bradley, L., Sipocz, B., Robitaille, T., et al. 2019, *astropy/photutils*: v0.7
- Burgasser, A. J. 2004, *ApJS*, 155, 191, 191
- Burgasser, A. J., Gelino, C. R., Cushing, M. C., & Kirkpatrick, J. D. 2012, *ApJ*, 745, 26, 26
- Burgasser, A. J., Gillon, M., Melis, C., et al. 2015, *AJ*, 149, 104, 104
- Burrows, A., Sudarsky, D., & Lunine, J. I. 2003, *ApJ*, 596, 587, 587
- Caselden, D., Westin, Paul, I., Meisner, A., Kuchner, M., & Colin, G. 2018, *WiseView: Visualizing motion and variability of faint WISE sources*, ascl:1806.004
- Cushing, M. C., Kirkpatrick, J. D., Gelino, C. R., et al. 2011, *ApJ*, 743, 50, 50
- Debes, J. H., Thévenot, M., Kuchner, M. J., et al. 2019, *ApJL*, 872, L25, L25
- Dupuy, T. J., & Kraus, A. L. 2013, *Science*, 341, 1492, 1492
- Dupuy, T. J., & Liu, M. C. 2012, *ApJS*, 201, 19, 19
- Dupuy, T. J., Liu, M. C., & Leggett, S. K. 2015, *ApJ*, 803, 102, 102
- Dupuy, T. J., Liu, M. C., Best, W. M. J., et al. 2019, *AJ*, 158, 174, 174
- Dye, S., Lawrence, A., Read, M. A., et al. 2018, *MNRAS*, 473, 5113, 5113
- Eisenhardt, P. R. M., Marocco, F., Fowler, J. W., et al. 2019, *arXiv e-prints*, arXiv:1908.08902, arXiv:1908.08902
- Esplin, T. L., Luhman, K. L., Cushing, M. C., et al. 2016, *ApJ*, 832, 58, 58
- Faherty, J. K., Burgasser, A. J., Cruz, K. L., et al. 2009, *AJ*, 137, 1, 1
- Faherty, J. K., Tinney, C. G., Skemer, A., & Monson, A. J. 2014, *ApJL*, 793, L16, L16
- Faherty, J. K., Burgasser, A. J., Walter, F. M., et al. 2012, *ApJ*, 752, 56, 56
- Faherty, J. K., Goodman, S., Caselden, D., et al. 2019, *arXiv e-prints*, arXiv:1911.04600, arXiv:1911.04600
- Gennaro, M. et al. 2018,
- Gonzaga, S., Hack, W., Fruchter, A., & Mack, J. 2012,
- Hanel, R., Conrath, B., Herath, L., Kunde, V., & Pirraglia, J. 1981, *J. Geophys. Res.*, 86, 8705, 8705
- Jeans, J. H. 1902, *Philosophical Transactions of the Royal Society of London Series A*, 199, 1, 1
- Joye, W. A., & Mandel, E. 2003, *Astronomical Society of the Pacific Conference Series*, Vol. 295, *New Features of SAOImage DS9*, ed. H. E. Payne, R. I. Jedrzejewski, & R. N. Hook, 489
- Kirkpatrick, J. D., Cushing, M. C., Gelino, C. R., et al. 2013, *ApJ*, 776, 128, 128
- Kirkpatrick, J. D., Gelino, C. R., Cushing, M. C., et al. 2012, *ApJ*, 753, 156, 156
- Kirkpatrick, J. D., Kellogg, K., Schneider, A. C., et al. 2016, *ApJS*, 224, 36, 36
- Kirkpatrick, J. D., Martin, E. C., Smart, R. L., et al. 2019, *ApJS*, 240, 19, 19
- Kuchner, M. J., Faherty, J. K., Schneider, A. C., et al. 2017, *ApJL*, 841, L19, L19
- Lang, D. 2014, *AJ*, 147, 108, 108
- Leggett, S. K., Marley, M. S., Freedman, R., et al. 2007, *ApJ*, 667, 537, 537
- Liu, M. C., Dupuy, T. J., & Allers, K. N. 2016, *ApJ*, 833, 96, 96
- Liu, M. C., Dupuy, T. J., Bowler, B. P., Leggett, S. K., & Best, W. M. J. 2012, *ApJ*, 758, 57, 57
- Lodders, K., & Fegley, B. 2002, *Icarus*, 155, 393, 393
- Low, C., & Lynden-Bell, D. 1976, *MNRAS*, 176, 367, 367
- Luhman, K. L. 2014, *ApJL*, 786, L18, L18
- Luhman, K. L., Burgasser, A. J., & Bochanski, J. J. 2011, *ApJL*, 730, L9, L9
- Luhman, K. L., & Esplin, T. L. 2014, *ApJ*, 796, 6, 6
- . 2016, *AJ*, 152, 78, 78
- Luyten, W. J. 1922, *Lick Observatory Bulletin*, 336, 135, 135
- MacKenty, J. W., Kimble, R. A., O’Connell, R. W., & Townsend, J. A. 2008, in *Society of Photo-Optical Instrumentation Engineers (SPIE) Conference Series*, Vol. 7010, *Proc. SPIE*, 70101F
- Mainzer, A., Grav, T., Bauer, J., et al. 2011, *ApJ*, 743, 156, 156
- Mainzer, A., Bauer, J., Cutri, R. M., et al. 2014, *ApJ*, 792, 30, 30
- Makovoz, D., & Marleau, F. R. 2005, *PASP*, 117, 1113, 1113
- Mamajek, E. E., Barenfeld, S. A., Ivanov, V. D., et al. 2015, *ApJL*, 800, L17, L17
- Marocco, F., Caselden, D., Meisner, A. M., et al. 2019, *ApJ*, 881, 17, 17
- Marocco, F., Kirkpatrick, J. D., Meisner, A. M., et al. 2020, *ApJL*, 888, L19, L19
- Martin, E. C., Kirkpatrick, J. D., Beichman, C. A., et al. 2018, *ApJ*, 867, 109, 109
- McKinney, W. 2013, *Python for Data Analysis: Data Wrangling with Pandas, NumPy, and IPython*, 1st edn.
- McMahon, R. G., Banerji, M., Gonzalez, E., et al. 2013, *The Messenger*, 154, 35, 35
- Meisner, A. M., Lang, D., & Schlegel, D. J. 2017a, *AJ*, 154, 161, 161
- . 2017b, *AJ*, 153, 38, 38

- . 2018a, *AJ*, 156, 69, 69
- Meisner, A. M., Lang, D. A., & Schlegel, D. J. 2018b, *Research Notes of the American Astronomical Society*, 2, 202, 202
- Meisner, A. M., Caselden, D., Kirkpatrick, J. D., et al. 2020, *ApJ*, 889, 74, 74
- Morley, C. V., Fortney, J. J., Marley, M. S., et al. 2012, *ApJ*, 756, 172, 172
- Morley, C. V., Marley, M. S., Fortney, J. J., & Lupu, R. 2014a, *ApJL*, 789, L14, L14
- Morley, C. V., Marley, M. S., Fortney, J. J., et al. 2014b, *ApJ*, 787, 78, 78
- Morley, C. V., Skemer, A. J., Miles, B. E., et al. 2019, *ApJL*, 882, L29, L29
- Morley, C. V., Skemer, A. J., Allers, K. N., et al. 2018, *ApJ*, 858, 97, 97
- Padoan, P., Kritsuk, A., Michael, Norman, L., & Nordlund, Å. 2005, *Mem. Soc. Astron. Italiana*, 76, 187, 187
- Padoan, P., & Nordlund, Å. 2002, *ApJ*, 576, 870, 870
- Padoan, P., Nordlund, Å., Kritsuk, A. G., Norman, M. L., & Li, P. S. 2007, *ApJ*, 661, 972, 972
- Pinfield, D. J., Gromadzki, M., Leggett, S. K., et al. 2014, *MNRAS*, 444, 1931, 1931
- Rees, M. J. 1976, *MNRAS*, 176, 483, 483
- Reipurth, B., & Clarke, C. 2001, *AJ*, 122, 432, 432
- Robitaille, T., & Bressert, E. 2012, *APLpy: Astronomical Plotting Library in Python*, ascl:1208.017
- Saumon, D., Marley, M. S., Abel, M., Frommhold, L., & Freedman, R. S. 2012, *ApJ*, 750, 74, 74
- Schneider, A. C., Cushing, M. C., Kirkpatrick, J. D., & Gelino, C. R. 2016, *ApJL*, 823, L35, L35
- Schneider, A. C., Cushing, M. C., Kirkpatrick, J. D., et al. 2015, *ApJ*, 804, 92, 92
- Scholz, R.-D. 2014, *A&A*, 561, A113, A113
- Silk, J. 1977a, *ApJ*, 214, 152, 152
- . 1977b, *ApJ*, 214, 718, 718
- Skemer, A. J., Morley, C. V., Allers, K. N., et al. 2016, *ApJL*, 826, L17, L17
- Skrutskie, M. F., Cutri, R. M., Stiening, R., et al. 2006, *AJ*, 131, 1163, 1163
- Stamatellos, D., & Whitworth, A. P. 2009, *MNRAS*, 392, 413, 413
- Stetson, P. B. 1987, *PASP*, 99, 191, 191
- Tinney, C. G., Faherty, J. K., Kirkpatrick, J. D., et al. 2014, *ApJ*, 796, 39, 39
- . 2012, *ApJ*, 759, 60, 60
- Tinney, C. G., Kirkpatrick, J. D., Faherty, J. K., et al. 2018, *ApJS*, 236, 28, 28
- Visscher, C., Lodders, K., & Fegley, Bruce, J. 2006, *ApJ*, 648, 1181, 1181
- Whitworth, A. P., & Zinnecker, H. 2004, *A&A*, 427, 299, 299
- Wright, E. L., Eisenhardt, P. R. M., Mainzer, A. K., et al. 2010, *AJ*, 140, 1868, 1868
- Zalesky, J. A., Line, M. R., Schneider, A. C., & Patience, J. 2019, *ApJ*, 877, 24, 24